OPEN ACCESS

University of BRISTOL

Dias Paulino Da Costa, F., Gaitonde, A. L., & Jones, D. P. (2021). *Virtual Experiments of Light and Shock Wave Interaction Using Nonlinear Ray Tracing and Photon Mapping*. https://doi.org/10.2514/6.2021-1483

Peer reviewed version

Link to published version (if available):
10.2514/6.2021-1483

Link to publication record in Explore Bristol Research
PDF-document

This is the author accepted manuscript (AAM). The final published version (version of record) is available online via AIAA at https://doi.org/10.2514/6.2021-1483. Please refer to any applicable terms of use of the publisher.

University of Bristol - Explore Bristol Research
General rights

This document is made available in accordance with publisher policies. Please cite only the published version using the reference above. Full terms of use are available:
http://www.bristol.ac.uk/red/research-policy/pure/user-guides/ebr-terms/

Virtual Experiments of Light and Shock Wave Interaction Using Nonlinear Ray Tracing and Photon Mapping

Frederico D. P. da Costa*, Ann L. Gaitonde†, and Dorian P. Jones‡
Department of Aerospace Engineering
University of Bristol
University Walk
Bristol
BS8 1TR

Light impinging on an aircraft wing surface interacts with the shock waves that form around it due to the high-speed flow and produces an oscillatory optical phenomenon composed of image distortions or shadow patterns, visible from the airborne perspective under particular observer, vehicle operation and illumination conditions. Analogously to traditional experimental techniques of shock wave visualization, the phenomenon can in principle be replicated computationally in its entirety, although the exact conditions that make it visible are still unknown. From a virtual experiment, it remains to be established what can be inferred about the shock wave and the trans-super sonic flow itself from the observed visual artifacts. This paper develops a three-dimensional nonlinear ray equation solver to predict the light propagation from the sun, through the refractive inhomogeneous density field acquired from a two-dimensional computational fluid dynamics (CFD) simulation and assembled as a pseudo-three-dimensional flow domain, to the physically-based reflective wing surface. Employing the traditional linear ray tracing algorithm, the photon mapping rendering technique and a simplified viewing system implementation, this computational tool is then used to assess the differences in the scene illumination caused by the shock wave. The contrast between the reflected radiance values, represented as a color triplet in the RGB space, considering the aerodynamic inhomogeneous flow field and a fictitious homogeneous optical medium demonstrates that the shock wave indeed induces radiometric disturbances. A strategically positioned and oriented recording film is able to capture magnified deflections of light rays and samples of the density of photons result in the reproduction of the shock wave's shadow formation. Visualized as in the shadowgraphy experiment or observed from a perspective around the aircraft wing, the characteristics of the shadow pattern depend on the number of photons and the direction that they are emitted from the light source.

I. Introduction

The interaction between sunlight and compressible flow gives rise to an optical effect on the aircraft wing related to the presence of shock waves and the corresponding disturbed thermodynamic field. In the out-of-the-window view it is possible to see some blurs or a pair of bright and dark stripes, attached to the wing surface and moving as the transonic flight progresses (see videos: [1–3], with screenshots captured in Figure 1). However, these phenomena are only visible under certain lighting conditions and from a favourable viewing position [2, 4].The question arises: what can be inferred about the shock wave and the flow field itself from the observed shadow pattern and distortions?

Although in-flight shock wave visualization is relatively rare, the effect that a compressible flow field exerts over light has already been extensively explored in aerospace research to generate images of aerodynamic features by means of optical mechanisms. By transmitting a light beam through optically and thermodynamically inhomogeneous air in an experiment, the resulting displacement, deflection angle or phase change of the light ray enabled the first visualization of shock waves, considered until then invisible. Shadowgraph, schlieren and interferometer imaging represent, respectively, these three classes of flow visualization methods [5]. Settles and Hargather [6] provided a comprehensive review of the developments undergone by these optical techniques that have played a major role in "wind-tunnel testing and the

*PhD Student, Department of Aerospace Engineering, f.paulino@bristol.ac.uk.
†Reader in Aerodynamics, Department of Aerospace Engineering, ann.gaitonde@bristol.ac.uk.
‡Reader in Aerodynamics, Department of Aerospace Engineering, dorian.jones@bristol.ac.uk.

(a) (b) (c)

Fig. 1 Image distortions (1a and 1c) and shadow pattern (1b) due to shock waves visible during transonic flight. The images are from [1–3] and are in the public domain.

development of high-speed aircraft" [6]. More recently the invention of digital high-speed video cameras has enabled the engineering of new flow visualization methods, such as the synthetic or background-oriented schlieren (BOS) [6]. This technique has been developed for in flight testing by NASA's Armstrong Flight Research Center who have captured impressive images with their Air-to-Air Background Oriented Schlieren (AirBOS) system [7].

From the advent of the computer, researchers started using the same principles of the traditional techniques in a new approach to flow visualization, now performed entirely in a virtual environment with no need for experimental apparatus, according to the chronological presentation provided by Havener [8]. Following the forward modelling approach [9], CFD solvers with diversified accuracy and complexity handling capabilities have been used to model various compressible flow phenomena, and the Computational Flow Imaging (CFI) science of "generating digital images of theoretical fluid dynamic phenomena" "that simulate real observations" [8] has been applied alongside to model the measurement process and, thus simulate a complete physical observation.

By evaluating and integrating functions of the index-of-refraction along the line of sight [10], using well known numerical edge or discontinuity detection techniques [11], tracing light rays through the fluid flow domain and the optical system [9, 12], or mapping the photons distribution after the tracing process [13], numerical analogous of schlieren, shadowgraph and interferogram images were generated [9–14]. Assumptions regarding the light behaviour ranged from minimal deflections and straight path perpendicular to the image plane [10], linear propagation within mesh elements and refraction at respective boundaries captured by the Snell's Law [12], to none at all and full governing equation solution [9, 13]. These synthetic images enabled mainly the verification and validation of CFD and CFI simulations via direct comparison to experimental images of the same nature, saving time and money that would otherwise be spent with the planning, execution and evaluation of those experiments.

With the ongoing advancements in high-performance computing, CFI is currently still being further developed to not only validate CFD and CFI codes via comparison with experimental data, but also provide an alternative to CFD post processing, study and predict real fluid dynamics problems and plan and assess experimental methods [8]. Among other advantages, the versatility of digital image processing, including options of computer zooming, perspective viewing, domain isolation and picture treatment, attracts the researchers given the possibility of extraction of some additional knowledge [8]. Nonetheless, there still exist a gap in the investigation and reproduction of the shadow pattern formation over wings of aircraft in high-speed flight, due to the presence of shock waves.

The developments of CFI facilitated a numerical investigation in this direction [15]. Onnink [15] used a combination of simplified two-dimensional ray tracing algorithm and transonic CFD model in an attempt to evaluate the behaviour of sun light impinging on an airfoil after passing through a shock wave and to subsequently reproduce the shadow pattern formed over the aerodynamic surface. The results of the study [15] showed that the characteristics of the shadows depend on the flow conditions and on the properties selected for the rendering analysis. However an unique relation between the light and shock wave properties could not be established, due to the limitations of the adopted approach.

Whilst answering the shock-shadow relation question is the longer term aim of this research programme, this study firstly builds on the recommendations for further developments of the analysis [15] and addresses most of the simplifying assumptions that limited the accurate representation and simulation of nature. The physical problem of

interest is recognised as three-dimensional, as in reality, and a more accurate compressible, viscous and transient fluid flow solution is predicted employing an open-source CFD software. The modelling of the light source, reflective surface and viewing system is performed using the concept of photon map, physically-based properties of real materials and a sensor-like image plane, respectively. A gradient-index ray tracing algorithm is developed to investigate the light ray propagation and refraction from the emitting Sun to the wing, whereas the traditional linear method is applied to evaluate the traversal from the reflective wing to the sensor. The geometrical optics field of study therefore provides the required framework to construct a computer simulation of light and a possibly viable aerodynamic data analysis tool stemming from digital image processing.

II. Flow Prediction

The computational fluid dynamics data is obtained through the open-source software OpenFOAM® [16] for transonic flow over a NACA 0012 airfoil. This is a well documented uncambered symmetric aerodynamic shape and is available as a standard tutorial case within OpenFOAM® package. The code solves the unsteady Reynolds Averaged Navier-Stokes (RANS) compressible flow equations using a combination of the Pressure Implicit with Splitting of Operator (PISO) and the Semi-Implicit Method for Pressure-Linked Equations (SIMPLE) iterative solvers, the so-called PIMPLE (rhoPimpleFOAM) algorithm [17], with the solution iterated until a steady flow is reached. This scheme has stability advantages with respect to the time step selection for the simulation. A k-Omega SST model is used to model turbulent fluctuations in the flow [18].

In a quasi-2D mesh composed of 32480 points and 16000 cells, containing only a single subdivision in the span-wise (third) dimension as requested by the software, the initial conditions of velocity ($U = 277m/s$), temperature ($T = 298K$) and pressure ($p = 10^5 N/m^2$) are enforced at the farfield, whilst a boundary condition of the type wall, or no velocity, is applied to the airfoil positioned at at an angle-of-attack of $\alpha = 0°$. From an imposed freestream Mach number of $M = 0.8$, the steady state solution in terms of air density, shown in Figure 2, is stored.

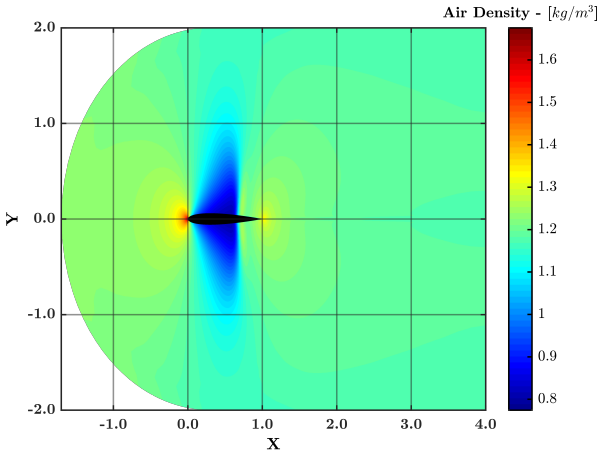

Fig. 2 Steady state solution of transonic flow over a NACA 0012 airfoil in terms of air density.

A. Constrained Tetrahedralization

Focusing only on the region of interest, the upper left section of the domain containing the flow upstream and over the upper surface of the airfoil including the shock wave, the air density values at the vertices of the quasi-2D mesh are thereafter replicated in six layers oriented along the remaining coordinate direction. This new isolated pseudo-three-dimensional flow domain composed of 41310 points then constitutes the basis for construction of a Constrained Delaunay Tetrahedralization (CDT) containing 201600 cells, here implemented using a multi-stage process involving Matlab®, Tetgen®, ParaView® and CGAL®. The use of constrained tetrahedralizations in computer graphics has already been reported [19] and Tetgen® is usually the popular, if not only, choice of open source software available for this meshing purpose. However, a script that performs data conversion between Tetgen® and CGAL®, the latter a well-known computational geometry library, has never been made available. The current script will be made available

for use as part of this research programme.

III. Photon Emission

Photons, the carriers of the light power or radiant flux (energy per unit time), are generated at the source location at the upper limit of the flow domain, region strictly above the wing. Each light particle is assigned with an equal fraction of the total power [20], a radiometric quantity (see section V) represented as a color triplet in the RGB space, each element respectively capturing the lower (blue), middle (green) and upper (red) wavelengths of the visible spectrum, enough to account for the spectral dependence of the illumination and map the spectral power distribution with regards to a human observer, according to the tristimulus theory of color perception [21]. The photons originate at evenly distributed positions along the x-coordinate direction and are emitted in a single global direction. This directional light source approximation although non-physical is acceptable to model the Sun characteristics [20].

In the shock wave's shadow nonlinear phenomenon, the drawback of employing a only traditional ray tracing technique is the complexity or possibly even the inability of connecting the two stages of light propagation, from the source to the surface and from the surface to the viewing system. Employing either the forward or the backward approach, one would be faced with the same challenge of "given two points in space, find a curved ray that obeys the underlying laws of nonlinearity and passes through the two defining points" [22]. In backward linear ray tracing, the shadow rays originate at intersection points at the surface and are directed towards light sources, providing a useful test for determination if this point is in shadow if the ray is blocked by another geometrical object. Given the nonlinearity, this direction is not easily determined anymore, the shadow ray may not even exist and the shadowing effect is due to light shift, instead of simple light blockage [22]. Therefore, radiometric variations would only be visible on the wing provided that the CFD mesh density was sufficiently refined in both the flow field and the solid surface, in order to capture detailed refractive shock and wing reflective surface shapes, and the sampling rate was accordingly defined to detect the effect of these surfaces on light behaviour. Otherwise, a converged solution would be only characterised by considerable variance, intrinsic to the method, making the shadow pattern negative and positive lighting peaks indistinguishable and the emission of more light rays would only be a waste of computational effort.

The combination of ray tracing with the photon mapping concept [20] recovers the generality of the rendering algorithm. Developed with the main goals of increased computational efficiency, complexity handling and noise reduction in the image synthesis, photon mapping is still a transport algorithm based on ray-tracing, employing ray geometrical optics to describe scattering and capable of sampling the continuous light from both ends of the light propagation. The flexibility of bidirectional path tracing and the "decouple of the representation of the illumination from the geometry" [20] are then attractive advantages, presenting the opportunity to explore the cached light paths and resulting lighting over the wing from different perspectives, considering constraints in terms of light source and viewing system and given a now consistent solution that will converge if the number of photons being emitted is increased. The reconstruction of the illumination now using a statistical density estimation approach is the key to the shock wave's shadow simulation.

IV. Light Propagation and Refraction

The idea behind ray tracing has been used for a long time in optics to design lenses [23] through the analysis and evaluation of the paths followed by light rays in optical systems. Following the same principles, a computer graphics technique that adopts the same name has found its niche in the generation of digital or synthetic two-dimensional pictures of the three-dimensional world [24]. This process has traditionally embedded the assumption that light rays propagate in linear trajectories. When it comes to refraction this phenomena has been modeled simply by applying Snell's Law [25] at the boundaries of objects, or between different media of constant refractive index [26, 27].

However, in a gradient-index media the index-of-refraction is not constant or homogeneous, but varies continuously in space [27]. This situation arises in compressible aerodynamics and light rays propagate along nonlinear trajectories (curved paths) [27, 28]. In practice, it is usually impossible to accurately predict the profile of refractive index, reason why the mathematical equation that governs the behaviour of light in optical media has to be solved in order to obtain the light path, at least approximately.

A. Nonlinear Ray (or Photon) Tracing

Some authors attempt to simplify the ray tracing process by classifying distinctive types of optical property distributions [23, 29, 30] or deriving analytical light ray paths [26, 27], however these studies make assumptions

regarding the spatially varying media that are too restrictive. In more general physical simulations, the alternative is to obtain the nonlinear light ray path via integration of the light ray equation coming from the geometrical optics domain. A number of different numerical schemes appear in the literature [26], however most of the approaches involve a piecewise linear approximation of the light rays [27]. This concerns an assumption of locally constant index-of-refraction within each integration step, which constrains the step size required for accurate solution and can lead to high computational costs [26].

This paper avoids any simplifying assumptions with respect to the refractive index of the media and only attempts to model the light behaviour by solving the Ray Equation through coupled numerical gradient estimation, interpolation and integration techniques based on an underlying discrete representation of the flow field domain.

B. Ray Equation

The ray equation is derived using Fermat's Principle and Calculus of Variations [31] and is given by

$$\frac{d}{ds}\left(n\left(\mathbf{r}\right)\frac{d\vec{\mathbf{r}}}{ds}\right)=\nabla n\left(\mathbf{r}\right) \tag{1}$$

The solutions of the ray equation (Equation 1) for an Isotropic Inhomogeneous Medium are the particular parametric curves $\vec{r}(t)=\langle x(t),y(t),z(t)\rangle$ that minimize the optical path length or, reciprocally, solve the variational calculus problem by satisfying the Euler equations, therefore providing the paths adopted by the light rays in nonlinear media.

Treating a light beam as an electromagnetic wave propagation phenomenon through a fluid flow that is characterized as isotropic inhomogeneous in terms of varying fluid density [5], the preliminary studies of Clausius and Mossotti and of Lorentz and Lorenz [32] resulted in formulae, that relate the refractive index of the fluid to its density, according to the properties of an electron, molecular constants and properties of the fluid and oscillatory features of the light considered.

Given that the refractive index of common gases is approximately equal to unity, these formulae can be further simplified to the abbreviated Gladstone-Dale relation

$$n-1=K\rho \tag{2}$$

where K is the Gladstone-Dale constant. Table 1 presents the dependence of this constant on the wavelength of light across a range of values which includes the visible spectrum for air. As observed in Table 1, the wavelength of light in and at the vicinity of the visible spectrum does not strongly influence the Gladstone-Dale constant's value for the air, and the average value of $0.2276\left[cm^3/g\right]$ is used throughout the present work, instead of considering the mixture composition of the gas as a means to estimate this value.

Table 1 Gladstone-Dale constant for air at T=288 $[K]$

K$\left[cm^3/g\right]$	Wavelength$[\mu m]$
0.2239	0.9125
0.2250	0.7034
0.2259	0.6074
0.2274	0.5097
0.2304	0.4079
0.2330	0.3562

As detailed by Sakamoto [33], algorithms to approximately solve the Ray Equation can be developed based on a change of the independent variable that describes the ray. For this transformation, a new variable, t, is written in terms of the arc length along the ray or simply ray path, s, and a power of the refractive index, n^k. One of the main references in ray tracing methods for gradient-index media [28] concerns the case in which $k=-1$ and the new independent variable is called the quasi-ray path [33].

Following Sharma et al. [28] the equation for t is

$$t=\int\frac{1}{n}ds \tag{3}$$

and hence dt is given by

$$dt=\frac{ds}{n} \tag{4}$$

Then using these substitutions in Equation 1 yields a new system of two ordinary differential equations

$$\frac{d^2\vec{r}}{dt^2} = n\nabla(n) = \frac{1}{2}\nabla\left(n^2\right) \tag{5}$$

$$\frac{d\vec{r}}{dt} = \vec{T} = n\cos(\alpha)\,\vec{i} + n\cos(\beta)\,\vec{j} + n\cos(\gamma)\,\vec{k} \tag{6}$$

These equations can be solved iteratively to give the position of the light ray $\vec{r}$ and the tangent vectors $\vec{T}$ along its path.

C. Adaptive Solution of the Ray Equation

Runge-Kutta (RK) methods have been used extensively in optics to solve the ray equation due to their computational efficiency. In the widely cited paper by Sharma et al. [28], a simplified form of the standard fourth-order RK method [34] was used, with the ray equation rewritten as a system of two first-order differential equations. The simplification is possible due to the absence of a first derivative on the right hand side of the equation [35]. Alternative modified methods, such as Runge-Kutta-Nyström (RKN) [36], can be applied directly to the second order equations, which presents advantages in terms of computation time and memory requirements. The same characteristics that allows the simplification of standard integration routines also simplifies the derivation of the composing coefficients of RKN methods[36], a more general approach [37].

Although there exists a multitude of numerical integration schemes using the RKN approach [38–40], with different formulae, orders of accuracy and advantages depending on the aimed application, a more traditional and general work is due to Fehlberg [36]. Therefore, the scheme employed to integrate the ray equation in this research is the Runge-Kutta-Nyström 4(5) presented by Fehlberg [36], referred to in the rest of this paper as the Runge-Kutta-Fehberg (RKF) method.

Described as embedded formulas, this method provides two approximations with fourth and fifth orders of accuracy, respectively, using the same function evaluations for computational efficiency. The higher-order approximation is used to advance the subsequent steps,technique known as local extrapolation, and the difference between the two approximations is interpreted as an estimation of the local error in the position of the ray at each step. This error can then be used to establish an adaptive integration scheme with an automatic step size control and adjustment procedure, based on a preset error tolerance [41].

Alongside the embedded Runge-Kutta formulas available in [36], the adaptive integration setup also consists of a prescribed tolerance of $TOL = 1\text{e}{-9}$ for comparison with the local error. From a starting step size of $h_0 = 0.001$, proportional to the domain discretization, the step size control procedure automatically adjusts it based on the ratio between the tolerance and the truncation error and respective exponent of $1/5$, a safety factor of $fac = 0.9$ to increase the probability of acceptance of the error (and consequently the size) on the next step and control factors of $fac_min = 0.1$ and $fac_max = 1.5$ to contain the rate of decrease and increase of the size, respectively, according to suggestions of Hairer et al. [37]. Moreover, as also advised in [37], after every step size rejection the control factor fac_max is returned to the unit, considering that the size has to be decreased.

D. Gradient Estimation and Interpolation

When using the RKF method to solve the ray equation, for each integration step the gradient of the refractive index of the air squared, ∇n^2, has to be evaluated at five interdependent points along the light ray path. However, the calculation of ∇n^2 has not been addressed directly with respect to ray tracing algorithms [29], but rather in terms of specific applications in the fields of CFD and computer graphics. In ray tracing, accuracy and efficiency are imperative in the gradient vector reconstruction and interpolation processes in order to achieve a satisfactory solution of light behaviour within the gradient-index domain. Gradient evaluation can affect directly the speed and complexity of the integration scheme. This is especially so when the refractive index distribution is provided as a discrete data set [29], which is the case in the present study. If this optical property of the fluid is available as a set of vertex-based mesh values then the gradient field is estimated in two stages: first, ∇n^2 is evaluated at the discrete data set vertex locations and, secondly, the value of ∇n^2 at every point required to trace a light ray is then found via interpolation.

The most cited methods for gradient vector estimation are variants of the Green-Gauss (GG) [42, 43] and Least Squares (LSQR) [44–46]. In the present research, the GG and LSQR linear and quadratic (unweighted) vertical regressions (LVR and QVR, respectively) have been compared. Specific attention has been paid to accuracy and the

effects that the underlying data field and the local characteristics of the mesh (cell size, orientation and skewness) have over the general consistency of the methods. Based on this work, the LSQR QVR was selected for vertex-based gradient vector estimation, due to its robustness and has been coded according to the formulae given by Barth [44].

To obtain the gradient vector at any non-vertex point required the vector is interpolated. Given the importance of the accuracy and robustness of this interpolation, a number of the methods were evaluated: LSQR QVR applied to a cell and its respective neighbouring elements; Nearest-Neighbour (NN); Partition of Unity (PU) and Radial Basis Function (RBF). A simple analysis of performance led to the selection of RBF for gradient vector interpolation, due to its consistent continuity, and accuracy of interpolated values. The ALGLIB® C++ library then provided the respective algorithm implemented [47].

The setup of the ALGLIB® algorithm to interpolate the gradient vector of the index-of-refraction squared in spatial locations scattered within the three-dimensional unstructured mesh involves the tuning of three parameters: the radius of the Gaussian basis function or "size of the sphere of influence of the points with known function values", the number of layers through which the radius will be successively decreased to build a hierarchy of models and the regularization coefficient for noise smoothing control [47].

Taking into consideration the exact reproduction of the input data and fast RBF model construction and interpolation evaluation, the radius is then selected to be equal to the average of the mean distance of each vertice's nearest neighbors, with five layers and no smoothing. Although not exactly following the recommendations available in [47], previous interpolation test performed with the proposed setup provided to be enough for the current analysis.

E. Boundary conditions

Additional conditions are needed during gradient reconstruction to ensure the correct physical behaviour of light rays at boundaries such as the solid surface and the farfield. Flags are set to identify if the vertices, facets and cells of the mesh pertain either to the interior of the domain or to one of the boundaries. For cells at the farfield, the cell has fewer neighbours and thus the number of interior data points used to estimate the gradient vector is a naturally lower which can cause gradient estimation errors. This issue is overcome by increasing the number of neighbouring cells used in gradient estimation, i.e. using information from neighbours of neighbours. At a solid surface boundary it is important to identify when the integration step from the fluid domain leads to a point inside the solid surface and to treat gradient estimation differently in the vicinity of the body. This is achieved by using halo cells within the solid surface in which the density value is mirrored, a process similar to that used in many cell-centred CFD codes to enforce boundary conditions. This enforces a zero density gradient along the normal at the solid surface. This is a reasonable assumption for the present investigations when it is assumed that there is no significant heat transfer in this region.

F. Automatic Discontinuity Detection and Integration Refinement

The focus of this paper is on ray tracing for light passing through a shock wave or waves that form in high-speed flow over aerodynamic bodies. For much of the flow field the variations in density are negligible and the high density gradient region is confined to a, usually, thin region around the shock. This specific characteristic of high speed compressible flow is challenging for ray tracing solvers. The numerical integration scheme and its automatic step size control and adjustment procedure only handles local domain information, which can cause an issue when two adjacent integration points fall in the regions upstream and downstream of the shock wave where local variations in density at each point are very low, despite the difference between the density values at the two points being high. The zero gradient of density condition in the regions around each integration point leads to an integration truncation error in the RKF scheme that is below the preset tolerance. Thus the tracing continues without reduction of the step size, missing the shock discontinuity and, consequently, the physical light ray bending.

Therefore, a modified methodology has been implemented to ensure that the dramatic density change that occurs across a shock wave, a fundamental trait of this type of compressible flow phenomena [5], is detected and the step size reduced accordingly. The air density is checked continuously along a light ray path, by interpolating at the beginning and end of every step, with the percentage change between the two values compared to a preset threshold of density variation. If the percentage change exceeds the threshold, the shock density discontinuity has been clearly missed within the step. It is now detected and the current step is rejected as too large. A bisection approach is then taken to reduce the step so that a suitable smaller step size is identified, which yields a density percentage change across the step that lies within the threshold.

This corrects the integration so that both ends of the step are on the same side of the shock as the origin of the cast light ray. The new smaller step size is used to advance the numerical integration and provides a suitable level of

refinement across the shock wave. The interpolation of the air density along the integration path is performed using a Hyperplane fitting approach. This process is efficient even on unstructured polygonal meshes, which is a key requirement due to the number of times this interpolation is performed. The logic of the procedure is explained in Figure 3.

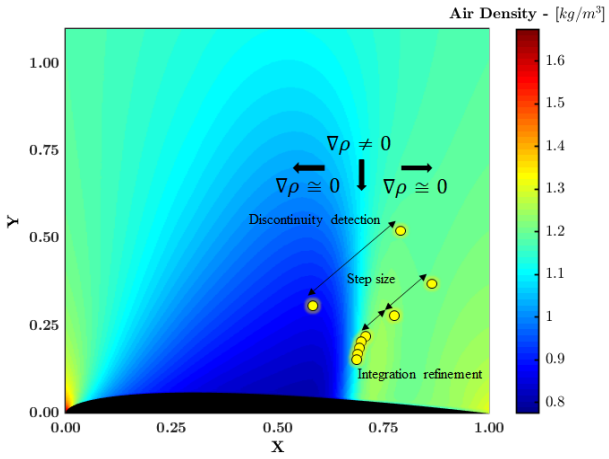

Fig. 3 Schematic of automatic discontinuity detection and integration refinement methodology.

G. Intersection of Light Rays with the Wing

The point at which a light ray leaves the flow domain and enters the solid surface during a step of the RKF scheme is detected using an internal function of the CGAL® library [48], which queries if a certain point is located inside or outside the constrained tetrahedralization. In order to obtain accurate results for the position of the intersection between a single light ray and the solid surface, the nonlinearity of the light ray path has to be accounted for since the density gradients in the boundary layer adjacent to the surface are high.

Following the technique devised by Fine [49] for Runge-Kutta-Nyström methods, the solution and its first and second-order derivatives at the beginning and end of an integration step are used to construct interpolation polynomials, or interpolants, a continuous intermediate trajectory between integration points. The ray position variable is then evaluated backwards, starting from the last computed integration point until it reaches the boundary between the aerodynamic body and the fluid flow. When this condition is established, the point is then considered to be inside the constrained tetrahedralization. The intersection between the light ray and the object is thus determined, along with the ray direction variable and the mesh cell in which the light ray hit the surface. This technique does not result in additional expensive computations, since all the information needed to compose the coefficients of the polynomials derive from the integration step, and the accuracy of the interpolants is relatively close to that of the inputs used in its derivation [49].

H. Photon Storing

When a light ray intersects the wing, the hit position and the incident direction (see subsection IV.G) along with the fraction of the emitted light power transported by the photon are stored in an exclusive data structured, named Photon Map [20]. As described by Jensen [20], this cached flux distribution can subsequently be used to evaluate both the incoming and the reflected lighting of the wing surface, through statistical analysis of the respective energy density.

V. Light Reflection

After being emitted from the directional light source and traced through the gradient-index medium, the photons interact with the wing and are either reflected or absorbed [20] (conductors - metals - "don't transmit light, but some of the incident light is absorbed by the material and turned into heat" [21]). In order to perform a physically-based simulation of light reflection from the wing, which together with the refraction that previously takes place are "macroscopic manifestations of scattering occurring on a submicroscopic level" [25], and accurately predict a realistic synthetic image that represents the shock wave's shadow scene, radiometry and respective electromagnetic radiation variables and principles are employed.

Forming the basis of rendering and global illumination algorithms [20, 21, 50], the radiance, or energy arriving at or leaving a point on a surface per unit time per unit area and per unit solid angle, is the variable of interested to be computed at the locations hit by the photons. Differently from the total flux or power emitted from the source and propagated via the photons, the radiance embodied by light rays change during refraction [20] and can be defined anywhere in the domain [50], which allows its evaluation on the wing surface itself or on a recording device, hence the availability of forward and backward ray tracing techniques.

As in the nonlinear photon tracing stage,the nature of light is again treated from the geometrical optics perspective, i.e. considering the dimension of the physical problem (shock wave formation over a wing) much larger than the light's wavelength [21, 25]. This way, the radiant energy behaviour at reflection is assumed to be linear, energy conserving and in the steady state [21], and diffraction and interference effects are neglected.

A. Reflection Equation

The reflection model thus evaluates the integral of the incident radiance (L_i) on a point (p), from all the directions ($\theta_i, \vec{\omega_i}$) in the hemisphere above it, and provides the radiance exiting back towards the domain (L_o) in a certain direction ($\vec{\omega_o}$), as depicted in the so-called Reflection Equation [20, 21, 50], written as

$$L_o\left(p, \vec{\omega_o}\right) = \int_{2\pi^+} f_r\left(p, \vec{\omega_i}, \vec{\omega_o}\right)\left[L_i\left(p, \vec{\omega_i}\right) cos\theta_i d\omega_i\right] \tag{7}$$

The variations of the wing visual appearance based on the directions that it is being lightened and viewed from are intrinsically present on the dependence of the radiances on these directions and, more importantly, on the formal abstraction that describes how a surface made of a certain material reflects light, the Bidirectional Reflectance Distribution Function or simply BRDF (f_r). Moreover, just as the illumination coming from light source, the spectral dependence of the reflected light is accounted for by representing both radiances and BRDFs also as colors in the RGB space. As shown in Equation 7, the BRDF is therefore the constant of proportionality between incident and exitant radiances.

B. Physically-Based Rendering

BRDFs formulae are devised from various types of sources, including experimental tests applied to real materials, pure qualitative analysis and description of the scattering phenomenon or even from a detailed wave or geometric optics framework, thus ranging in the level of complexity from tabular and readily available data to approximate or complex equations and respective solution procedures [21]. However, in order to be consider physically-based, the BRDF must not be composed only by simple perfect (ideal) diffuse or perfect specular components [20], but a combination of these two, glossy specular and retro-reflection, and possibly consider effects of anisotropy [21]. In addition, these function must embed the energy conservation principle and are usually based on the concept of microfacets [20, 21, 51].

An approach based on the geometric optics field of study, the microfacet surface model, as the name suggests, consider it to be composed of an statistical distribution of microscopic perfectly reflective mirrors [21, 51]. Each facet individual behaviour then contributes to the overall surface reflection and depend on, primarily, the facet set alignment or, in other words, the microscopic roughness of the surface [21, 51]. It also depends on local lighting effects, such as occlusion, shadowing and interreflection between facets [21] and on the amount of the incoming energy that is actually reflected, instead of absorbed or transmitted, distinguishing thus dielectric and conductor materials [51].

One of the most recent [21] microfacet models is due to Walter et al. [52], implemented in the present study. For the Fresnel term (F), distribution (D) and geometry (G) functions, which takes into account all the above-mentioned factors that the BRDF depend on, the Schlick approximation with aluminium base reflectivity at normal incidence, the Trowbridge-Reitz GGX type and the Smith's method with a combination of Schlick-Beckmann and GGX approximations are respectively used, following the didactic description provided by Vries [51]. The specific details of the model are thoroughly explained in [51, 52] and included references and are outside the scope of this paper. Using this physically-based BRDF the wing is therefore treated as a pure reflective material.

VI. Image Synthesis

The photon map itself and its energy distribution data already presents relevant information regarding the global illumination of the scene: the indicative of existence of a shadow pattern on the wing surface given by the shift in concentration of particles in between certain adjacent regions, in contrast to rest of the surface. However, the map lacks the phenomenological and perceptual aspects of radiometry, "the study of the propagation of electromagnetic radiation

in an environment" [20], and it does not ensure the representation of the shock wave's shadow as an observable feature. Similarly, the much easier estimation of irradiance (compared to radiance) by regarding the wing as a light sensor still wouldn't allow the reproduction of this image generated based on the incident flux density per unit surface area [50] in reality and, consequently, the validation of the virtual experiment would not be possible.

Therefore, the photon map has to be visualized via reflected radiance estimation [20]. In order to compute this radiometric quantity (L_r) at any point on the surface, the Reflection Equation (Equation 7) is rewritten in terms of the irradiance [20]. The incoming flux ($\Delta\Phi$) density is then approximated using the nearest neighbor statistics method, assuming an sphere of radius r around the point of interest x with K photons within it, and finally multiplied by the BRDF (subsection V.B), as presented in

$$L_r\left(x, \vec{\omega_o}\right) \approx \frac{1}{\pi r^2} \sum_{p=1}^{K} f_r\left(x, \vec{\omega_i}, \vec{\omega_o}\right) \Delta\Phi_p\left(x, \vec{\omega_i}\right) \tag{8}$$

A. Viewing System

Employing initially only forward ray tracing from the sun towards the wing, the radiance could then be estimated by considering a recording film shaped exactly as the wing and positioned right outside its boundary, in a way that all the reflection occurs in the directions normal to the surface and the reflected light rays only traverse an infinitesimal distance until they reach the film. This case is analogous to the wing regarded as a light sensor previously mentioned, although now it is considered to be sensitive to reflected radiance. However, an analysis of the lighting of the wing surface through this approach demonstrates that the degree of light rays deflection at the surface is not enough to produce a synthetic shadow and the noise in the resulting images, inherent to ray-tracing methods, is usually of the same order of magnitude than the expected disturbances in the radiance distribution.

The subsequent step in the viewing system development, although still simplified, is the positioning of the recording film, now appropriately defined as an image plane, a certain distance away from the boundaries of the domain, either farfield or solid surface. Inspired by the shadowgraphy experimental technique, by allowing the reflected light rays to travel further from the hit locations and measuring the contrast in the pixels, or difference between the radiance values computed considering homo and inhomogeneous refractive-index fields, the deflections become much more pronounced and a considerable difference is observable in the computational image. A practical viewing system (virtual pinhole camera [50]) and the backward ray tracing process usually from the eye point passing through the pixels to the wing considering nonlinearities is not yet implemented in the present study. Instead, as traditionally applied to the visualization of photons maps [20], a cheaper linear ray tracer is used to track the light back towards the pixels, in a forward manner. The linear traversal is true in the case of simulations of shadowgraphs [5], in which the light travels outside the wind tunnel in homogeneous air, but only an approximation for the case of real shock wave's shadow, where secondary refractions would occur. The image plane is oriented in the perfect mirror reflection direction of the linear light rays case, thus sensing any slight variation cause by the shock waves.

VII. Results

A simulated shadowgraph of the NACA0012 airfoil at a freestream Mach number of 0.8 is presented on Figure 4. Only from the minimal 5000 initial photons emitted from the source it is already possible to visualize the clear deflection of those traversing the shock wave towards downstream of it, generating a bright spot at the location where they reach the recording film and a dark spot where they were originally directed to. This can be further confirmed by locating the foot of the shock wave, in the space between the x-coordinates equal to 0.6 and 0.7 in which there is a strong density gradient, and relating this position to the line of demarcation between the shadow and lighting pattern. The effect that the rendering parameters selection has over the quality of the synthesized image is evident in the final color computed for the pixels, some of which are distinguishable in the shadowgraph. Increasing the number of emitted photons, reducing the pixel size, allowing for more photons to be used in the density estimation for radiance computation or even applying filters for noise reduction and rendering smoothing can improve the appearance of the synthetic shadowgraph.

The number of emitted photons affects the image generation only to a certain extent. Although a very large number of photons constituting the light is desirable from the point of view of accurate density estimation, allowing the largest possible sample size and smallest possible sampling area, it is still an averaging statistical process. Figure 5 shows the contrast at the image plane for different numbers of photons traced from the source aligned with the y-coordinate direction, i.e. vertically oriented towards the wing. The contrast is calculated by the difference between the radiance

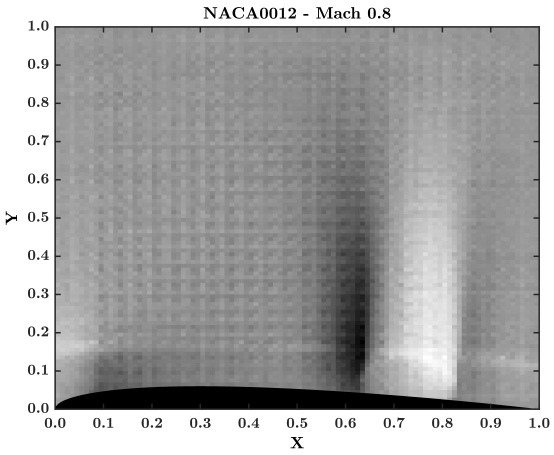

Fig. 4 Simulated shadowgraph of NACA 0012 at Mach 0.8**.**

values computed in two parallel simulations, one in an homogeneous optical medium (no flow nor shock wave) and the other concerning the aerodynamic test case. As it can be seen on the four lower plots, the emission of more than 10^3 photons provides only slight improvements in the colors estimation, smoothing out possible discontinuities in the values computed and numerical noise, compared to the four upper plots of reduced number of photons, where the progressive convergence in terms of density estimation and radiance computation is verified.

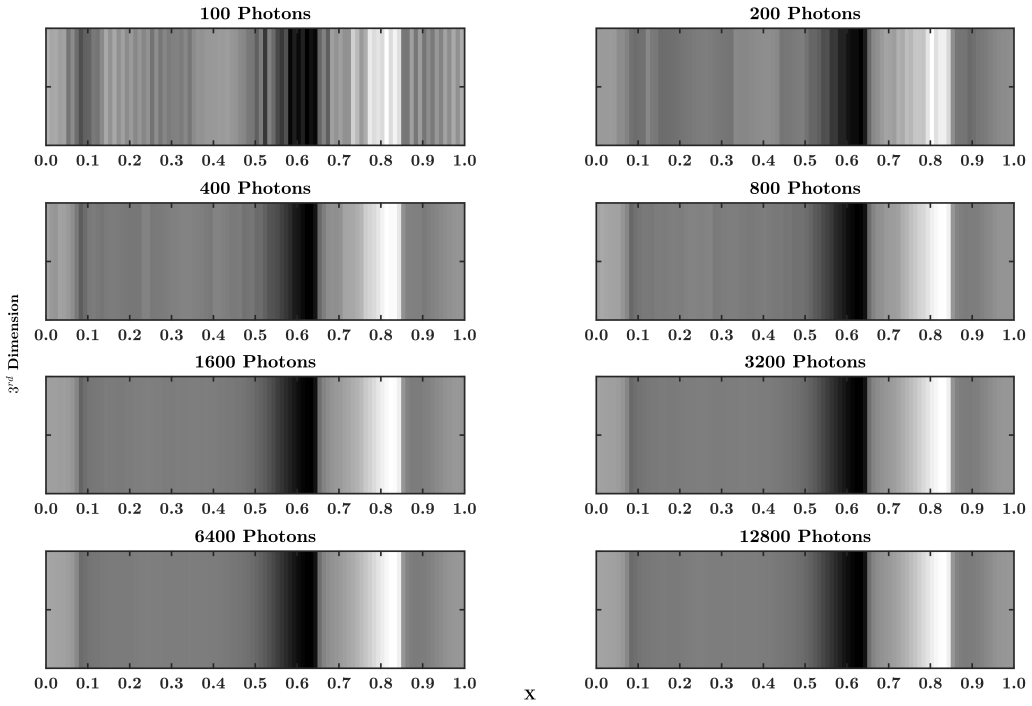

Fig. 5 Convergence of contrast due to increase number of emitted photons.

The Snell's Law of Refraction [25] prescribes the angle that a light ray will leave one side of the discontinuity between two different refractive index media based on the angle that it hits the other side. Analogously, the characteristics of the

shadow pattern are expected to depend on the direction of emission of the photons from the light source. To evaluate such dependence, light rays were cast at angles of ±20°, ±15°, ±10°, ±5° and 0° with respect to the y-coordinates direction or vertical and the resulting contrasts in the wing surface section are presented in Figure 6. Considering a clockwise rotation of the light rays from −20° to +20°, it is possible to realize that light rays that reach the shock surface with a more perpendicular orientation (at the lowest negative angles) produce shallow valleys and short peaks in the contrast curve, which translates to weak dark and bright spots in the synthetic shock wave's shadow image. As the light rays direction roughly aligns with the shock wave curvature (at zero and lowest positive angles), a grazing incidence occurs and the highest values of light deflection induce stronger shadow patterns, or deepest valleys and tallest peaks in the curves.

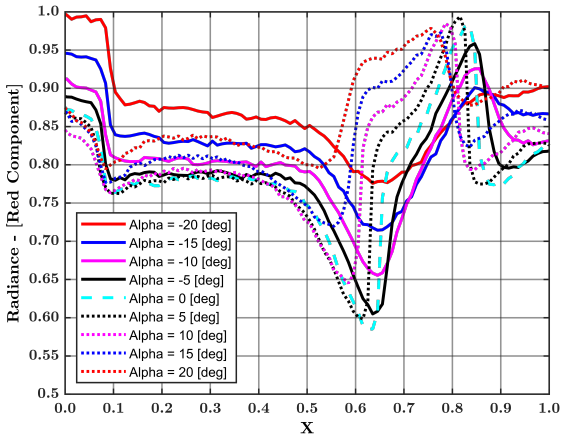

Fig. 6 Influence of light source direction over the resulting shadow pattern.

Given the photon density convergence study and the light source direction dependence analysis previously presented, the resultant shadow pattern formed over the wing assuming an emission of 1000 photons at the angle of 0° is shown on Figure 7.

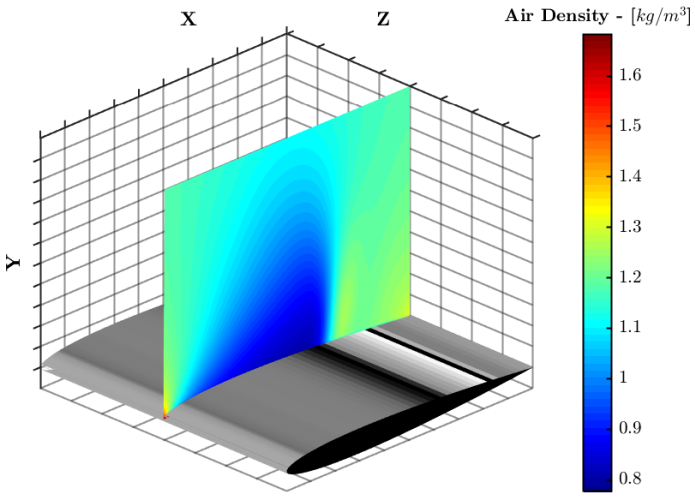

Fig. 7 Synthetic shock wave's shadow pattern over a NACA 0012 aerodynamically-shaped wing.

A. Discussion and Future Work

In this study, we have successfully designed a computational tool that employs carefully selected and efficient numerical methods to accurately simulate the behaviour of light within a compressible high-speed flow and synthesize images that exhibit the sought after effect, the shadow pattern produced by shock waves. This virtual experimental environment is the initial step towards establishing a relationship between aerodynamic and light phenomena and subsequently confirming the feasibility of extracting shock wave knowledge from observed shadows.

Even in this partial stage of development, the tool already provides researchers in Aerospace with the possibility of reproducing shock wave's shadow formation and visualizing it either from a wind tunnel or an airborne perspective, i.e. evaluating the resulting contrast on an image plane that can mimic a shadowgraph setup or a simplified recording device. The understanding that the nonlinearity characteristic of the light and shock wave interaction phenomenon requires the combination of ray tracing sampling-based technique and photon mapping density-estimation concept, and the realization that a strategic image plane position a certain distance from the region of interest reduces the exposition to which it is subjected and lead to enhanced light rays deflections, were the two main achievements that enable the visualization of shadow patterns at this stage.

To the best of our knowledge, this is the first published work to attempt to replicate the shock wave's shadow visualized in-flight. The majority of the studies in the field of computational flow imaging pursue the modelling of the optical setup of traditional flow visualization techniques, such as shadowgraphy and schlieren. However, without recurring to expensive and sophisticated resources, the methodology here developed is already able to simulate shadowgraphs and predict illumination aspects of the phenomenon that can happen in general transonic flight. This strongly suggests that the remaining details to be modelled are achievable and that the shock wave-shadow link is feasible, though still to be determined.

The viewing system modelled as a recording film exposed to a fictitious homogeneous optical medium is currently the major simplification of the approach. Without the implementation of a virtual camera and the nonlinear backward photon tracing process, the tool is still not able to fulfil all the requirements for reproducing every single aspect of the shadow visualization, identically to in reality. Moreover, the simulation of the phenomenon depends on the choices made with respect to parameters that control each and every operation of the numerical methods, from the CFD mesh density and solution, to light source and viewing system positioning and orientations, integration and interpolation tuning and final rendering characteristics. Therefore, an analysis of influence of all these factors on the final shadow image generated, will demand the application of acceleration techniques and possibly graphics hardware resources.

Future work will concern the practical modelling of the viewing system and subsequently include convergences analysis in terms of the CFD mesh and shock wave solution and again number of photons emitted and used in the density estimation. Although not shown here, the prediction of light propagation and refraction using the three-dimensional ray equation solver has already been validated in simple cases of refraction between two different media, analytically determined via the Snell's Law of Refraction. However, the prediction of light reflection through BRDFs and image synthesis process exploiting the photon map distribution have only been verified in the shadow images. Shadowgraph setups and respective images available in the literature could then be used to validate these two modules through direct comparison with simulated shadowgraphs. It is exactly the possibility of comparison between a real shadow recorded in-flight, an artificial shadow generated in a wind tunnel experiment and the computational shadow synthesized by the present methodology that governs the interests of this research, as either of the images and processes involved could be validated, alongside the referred study of shock waves from respective shadows. After all, as Havener wisely remembers, "a picture is worth a thousand words" [8] and when ready it will prove itself valuable to the whole scientific community.

B. Acknowledgements

References

[1] Kemper, G., "Transonic Shockwaves," , July 2009. URL `https://www.youtube.com/watch?v=JflaKnUNsPc&feature=emb_logo`.

[2] Croman, R., "Shock Wave Formation in Transonic Flight," , February 2016. URL `https://www.youtube.com/watch?v=HekbC6Pl4_Y`.

[3] bwalt822, "Standing Normal Shockwave on a 757 wing," , February 2009. URL `https://www.youtube.com/watch?v=aASdYfl08ck&feature=emb_logo`.

[4] Larmore, L., and Hall, F. F., "Optics for the airborne observer," *Optical Engineering*, Vol. 9, No. 3, 1971, p. 090387.

[5] Merzkirch, W., *Flow visualization*, Elsevier, 2012.

[6] Settles, G. S., and Hargather, M. J., "A review of recent developments in schlieren and shadowgraph techniques," *Measurement Science and Technology*, Vol. 28, No. 4, 2017, p. 042001.

[7] Kamlet, M., "NASA Captures First Air-to-Air Images of Supersonic Shockwave Interaction in Flight," , January 2019. URL `https://www.nasa.gov/centers/armstrong/features/supersonic-shockwave-interaction.html`.

[8] Havener, G., "Computational flow imaging: Fundamentals and History," *25th Plasmadynamics and Lasers Conference*, 1994, p. 2615.

[9] Luthman, E., Cymbalist, N., Lang, D., Candler, G., and Dimotakis, P., "Simulating schlieren and shadowgraph images from LES data," *Experiments in Fluids*, Vol. 60, No. 8, 2019, p. 134.

[10] Yates, L. A., "Interferograms, schlieren, and shadowgraphs constructed from real-and ideal-gas, two-and three-dimensional computed flowfields," 1992.

[11] Samtaney, R., Morris, R., Cheeseman, P., Sunelyansky, V., Maluf, D., and Wolf, D., "Visualization, extraction and quantification of discontinuities in compressible flows," 2000.

[12] Sun, M., "Computer modeling of shadowgraph optical setup," *27th International Congress on High-Speed Photography and Photonics*, Vol. 6279, International Society for Optics and Photonics, 2007, p. 62790L.

[13] Brownlee, C., Pegoraro, V., Shankar, S., McCormick, P., and Hansen, C. D., "Physically-based interactive flow visualization based on schlieren and interferometry experimental techniques," *IEEE transactions on visualization and computer graphics*, Vol. 17, No. 11, 2011, pp. 1574–1586.

[14] Zonglin, J., "Reliable validation based on optical flow visualization for CFD simulations," *Acta Mechanica Sinica*, Vol. 19, No. 3, 2003, pp. 193–203.

[15] Onnink, T., "Simulated Shadowgraphy of Transonic Wing-Bound Shock Waves," 2016.

[16] Ltd, O., "OpenFOAM The open source CFD toolbox: About OpenFOAM," , May 2020. URL `https://www.openfoam.com/`.

[17] SimScale, "CFD: PIMPLE Algorithm," , January 2018. URL `https://www.simscale.com/forum/t/cfd-pimple-algorithm/81418`.

[18] El Maani, R., Bouchaib, R., and El Hami, A., "CFD Analysis and Shape Optimization of NACA0012 Airfoil for Different Mach Numbers," *2019 5th International Conference on Optimization and Applications (ICOA)*, IEEE, 2019, pp. 1–6.

[19] Lagae, A., and Dutré, P., "Accelerating ray tracing using constrained tetrahedralizations," *Computer Graphics Forum*, Vol. 27, Wiley Online Library, 2008, pp. 1303–1312.

[20] Jensen, H. W., *Realistic image synthesis using photon mapping*, AK Peters/CRC Press, 2001.

[21] Pharr, M., Jakob, W., and Humphreys, G., *Physically based rendering: From theory to implementation*, Morgan Kaufmann, 2016.

[22] Gröller, E., "Nonlinear ray tracing: Visualizing strange worlds," *The Visual Computer*, Vol. 11, No. 5, 1995, pp. 263–274.

[23] Moore, D. T., "Gradient-index optics: a review," *Applied Optics*, Vol. 19, No. 7, 1980, pp. 1035–1038.

[24] Glassner, A. S., *An introduction to ray tracing*, Elsevier, 1989.

[25] Hecht, E., *Optics, 5e*, Pearson Education India, 2017.

[26] Cao, C., Ren, Z., Guo, B., and Zhou, K., "Interactive Rendering of Non-Constant, Refractive Media Using the Ray Equations of Gradient-Index Optics," *Computer Graphics Forum*, Vol. 29, Wiley Online Library, 2010, pp. 1375–1382.

[27] Mo, Q., Yeh, H., and Manocha, D., "Tracing analytic ray curves for light and sound propagation in non-linear media," *IEEE transactions on visualization and computer graphics*, Vol. 22, No. 11, 2015, pp. 2493–2506.

[28] Sharma, A., Kumar, D. V., and Ghatak, A. K., "Tracing rays through graded-index media: a new method," *Applied Optics*, Vol. 21, No. 6, 1982, pp. 984–987.

[29] Dorić, S., "Ray tracing through gradient-index media: recent improvements," *Applied optics*, Vol. 29, No. 28, 1990, pp. 4026–4029.

[30] Sands, P. J., "Classification scheme and nomenclature for refractive-index distributions," *Applied optics*, Vol. 22, No. 3, 1983, pp. 430–431.

[31] Stavroudis, O. N., *The mathematics of geometrical and physical optics: the k-function and its ramifications*, John Wiley & Sons, 2006.

[32] Born, M., and Wolf, E., *Principles of optics: electromagnetic theory of propagation, interference and diffraction of light*, Elsevier, 2013.

[33] Sakamoto, T., "Ray trace algorithms for GRIN media," *Applied optics*, Vol. 26, No. 15, 1987, pp. 2943–2946.

[34] Scraton, R., "The numerical solution of second-order differential equations not containing the first derivative explicitly," *The Computer Journal*, Vol. 6, No. 4, 1964, pp. 368–370.

[35] Collatz, L., *The numerical treatment of differential equations*, Vol. 60, Springer Science & Business Media, 2012.

[36] Fehlberg, E., *Classical eight-and lower-order Runge-Kutta-Nyström formulas with stepsize control for special second-order differential equations*, National Aeronautics and Space Administration, 1972.

[37] Hairer, E., and Wanner, G., "A theory for Nyström methods," *Numerische Mathematik*, Vol. 25, No. 4, 1975, pp. 383–400.

[38] Bettis, D., "A Runge-Kutta Nyström algorithm," *Celestial mechanics*, Vol. 8, No. 2, 1973, pp. 229–233.

[39] Cash, J. R., and Karp, A. H., "A variable order Runge-Kutta method for initial value problems with rapidly varying right-hand sides," *ACM Transactions on Mathematical Software (TOMS)*, Vol. 16, No. 3, 1990, pp. 201–222.

[40] Dormand, J., and Prince, P., "New Runge-Kutta algorithms for numerical simulation in dynamical astronomy," *Celestial Mechanics*, Vol. 18, No. 3, 1978, pp. 223–232.

[41] Hull, D. G., "Fourth-order Runge-Kutta integration with stepsize control," *AIAA Journal*, Vol. 15, No. 10, 1977, pp. 1505–1507.

[42] Barth, T., "Numerical aspects of computing high Reynolds number flows on unstructured meshes," *29th Aerospace Sciences Meeting*, 1991, p. 721.

[43] Nishikawa, H., "Beyond interface gradient: a general principle for constructing diffusion schemes," *40th Fluid Dynamics Conference and Exhibit*, 2010, p. 5093.

[44] Barth, T., "Recent developments in high order k-exact reconstruction on unstructured meshes," *31st Aerospace Sciences Meeting*, 1993, p. 668.

[45] Eberly, D., "Least squares fitting of data," *Chapel Hill, NC: Magic Software*, 2000.

[46] Neumann, L., Csébfalvi, B., König, A., and Gröller, E., "Gradient estimation in volume data using 4D linear regression," *Computer Graphics Forum*, Vol. 19, Wiley Online Library, 2000, pp. 351–358.

[47] ALGLIB®, "Fast RBF interpolation/fitting," , 2020. URL `https://www.alglib.net/interpolation/fastrbf.php`.

[48] Project, T. C., "CGAL The Computational Geometry Algorithms Library," , 2020. URL `https://www.cgal.org/`.

[49] Fine, J. M., "Interpolants for Runge-Kutta-Nyström methods," *Computing*, Vol. 39, No. 1, 1987, pp. 27–42.

[50] Suffern, K., *Ray Tracing from the Ground up*, CRC Press, 2016.

[51] de Vries, J., "Physically Based Rendering: Theory," , May 2020. URL `https://learnopengl.com/PBR/Theory`.

[52] Walter, B., Marschner, S. R., Li, H., and Torrance, K. E., "Microfacet Models for Refraction through Rough Surfaces." *Rendering techniques*, Vol. 2007, 2007, p. 18th.